Resonant Raman spectroscopy of 3,4,9,10-perylene-tetracarboxylic-dianhydride epitaxial films

R. Scholz, A.Yu. Kobitski, T.U. Kampen, M. Schreiber, and D.R.T. Zahn
Institut für Physik, Technische Universität, D-09107 Chemnitz, Germany

G. Jungnickel, M. Elstner, M. Sternberg, and Th. Frauenheim
Fachbereich Physik, Theoretische Physik, Universität Gesamthochschule Paderborn, D-33098 Paderborn, Germany
(Received 6 July 1999; revised manuscript received 7 December 1999)

We present a comprehensive investigation of Raman-active modes of 3,4,9,10-perylene-tetracarboxylic-dianhydride (PTCDA) thin films deposited on H-passivated Si(111) substrates. The experimental data are interpreted with a density-functional tight-binding scheme used for calculating the geometry and vibrational modes of the isolated molecule. These results for the breathing modes are applied to the optical absorption of PTCDA in solution, and the vibrational absorption bands can be related quantitatively to the elongation of the most prominent Raman modes during the highest occupied molecular orbital to lowest unoccupied molecular orbital transition. From a comparison of the calculated deformation of negatively charged $PTCDA^-$ with Raman spectra recorded in the region of the charge-transfer exciton, a significant net charge separation during the optical absorption is highly unlikely.

I. INTRODUCTION

In the last few years, various studies have focused on organic thin films due to their potentially interesting properties for electronic and optoelectronic applications such as electroluminescence diodes[1,2] or waveguide-coupled detectors.[3] After the recent developments of molecular beam deposition techniques adapted to these molecules, the growth of well-ordered organic thin films on different inorganic substrates has made enormous progress[4,5]. Among the molecules of interest, 3,4,9,10-perylene-tetracarboxylic-dianhydride (PTCDA) plays a special role because high quality films can be grown on different substrates with molecular beam deposition, and the resulting epilayers have been studied using a variety of techniques.[4]

The importance of internal vibrations for the optical properties of PTCDA has been evidenced in optical absorption measurements of PTCDA in solution and in epitaxial layers,[6] in fluorescence of epitaxial films,[7] and in fluorescence excitation spectra of dissolved molecules and amorphous films.[8] These pronounced vibrational structures have been interpreted in terms of a configuration coordinate diagram for a single effective vibrational mode of the molecule.[6,7] From group-theoretical arguments, only totally symmetric vibrations can be elongated due to the dipole-allowed optical transition from the electronic highest occupied molecular orbital (HOMO) to the lowest unoccupied molecular orbital (LUMO), the same symmetry restriction applying to resonant Raman scattering.

The purpose of the present work is to interpret recent measurements of resonant Raman scattering of PTCDA thin films[9] with a density-functional calculation of the vibrational properties of an isolated PTCDA molecule. In Sec. II, we introduce the density-functional tight-binding approach applied in the present work and investigate the geometrical changes of an isolated molecule after optical excitation. Details of the sample preparation, experimental setup, and resonance conditions are discussed in Sec. III. Section IV compares the measured Raman spectra with the calculated elongation patterns of PTCDA. In Sec. V, we apply these results to the linear absorption of PTCDA in solution. The paper is concluded in Sec. VI.

II. DENSITY-FUNCTIONAL TIGHT-BINDING THEORY

A. Theoretical model

PTCDA is composed of 38 atoms contributing 200 electrons. Such a large system requires an efficient theoretical approach including the main features of the electron-electron interaction, a computationally very efficient being density-functional theory (DFT) in the local-density approximation (LDA). As was shown recently in some detail, an even more efficient and simultaneously highly transferable tight-binding (TB) version of density-functional theory can be derived,[10] called density-functional tight-binding (DFTB) in the following.

The method is based on a second-order expansion of the Kohn-Sham total energy functional $E[n]$ with respect to charge-density fluctuations δn at a given reference density n_0, $n(\mathbf{r})=n_0(\mathbf{r})+\delta n(\mathbf{r})$. Retaining only the leading monopolar term of atom-centered charge fluctuations calculated by a Mulliken-charge analysis, one finally obtains an approximate tight-binding-like expression for the Kohn-Sham energy functional in second-order perturbation theory in the charge transfer:

$$E_2^{TB}[n]=\sum_i^{occ}\langle\Psi_i|\hat{H}_0|\Psi_i\rangle+E_{rep}[n_0]+\frac{1}{2}\sum_{\alpha,\beta=1}^{N}\gamma_{\alpha\beta}\Delta q_\alpha\Delta q_\beta. \quad (1)$$

The sum over the occupied eigenstates represents the leading matrix element of the many-atom Hamiltonian $\hat{H}_0$, and the second term stands for a short-range repulsive pair interaction, both taken at the reference density n_0 of N su-

perimposed neutral atoms. Besides the ion-ion repulsion, E_{rep} contains a correction for the double-counting Hartree and exchange-correlation contributions. The third term represents energetic contributions due to the net charge Δq_α of each atom α, and the distance laws $\gamma_{\alpha\beta}$ can be tabulated beforehand.[10]

The variational basis used consists of compressed atomiclike orbitals calculated in a self-consistent generalized gradient approximation[11] (GGA) using the Perdew-Burke-Ernzerhof[12] (PBE) density functional. From previous applications of this scheme[10] to 63 organic reference molecules, mean absolute deviations for the bond lengths of $\Delta R = 0.012$ Å and for bond angles of $\Delta\Theta = 1.80°$ where found, slightly more precise than in semiempirical AM1 calculations.[13] For vibrational frequencies, the mean absolute error for 33 reference molecules was found to be 6.4%, with a largest absolute error for each molecule of about 10%.[10,14]

Using a careful redefinition of the short-range repulsive energy E_{rep} between carbon atoms, a systematic deviation of vibrational frequencies by about 10% for graphitelike bond geometries could be eliminated. This empirical procedure improves the transferability and precision of the repulsive energy E_{rep} and its spatial derivatives for C−C bonds longer than about 1.35 Å , including the range needed for PTCDA.

B. Geometry of PTCDA

PTCDA is a planar rectangular molecule consisting of a carbon network terminated by hydrogen and oxygen, compare Fig. 1 for the HOMO and LUMO. The overall charge distributions shown agree qualitatively with earlier PM3 calculations for the HOMO[15] and ZINDO calculations for both HOMO and LUMO.[16]

For the geometry of an isolated PTCDA molecule, we have compared our DFTB results with a fully self-consistent density-functional calculation using the NRLMOL code,[17,18] based on the same PBE functional.[12] We found a rms deviation of the C−C and C=O bond lengths $<0.5\%$, defining a quite reasonable reference geometry for our DFTB calculation of the vibrational modes of the isolated molecule. The *peri* bonds between the two naphthalene units and also the bonds between the naphthalenes and the carboxylic groups are much longer than the bonds within the naphthalenes, as known from calculations for perylene[19] and observed in various other perylene pigments.[20]

The most significant deviation of the experimental PTCDA geometry in the bulk from the full D_{2h} symmetry of the isolated molecule is a pronounced assymetry of the different carboxylic bond lengths and an asymmetric distortion of the anhydride groups.[21,22] Furthermore, the bonds between the carboxylic groups and the naphthalene are considerably shortened. A detailed comparison of the calculated PTCDA geometry with experimental data for bulk phases will be published elsewhere.[23]

As the representations of the commutative group D_{2h} have eigenvalues $+1$ and -1 under the symmetry operations of the group, the square of each representation has eigenvalues $+1$ under all symmetry operations, or fully symmetric A_g transformation properties. Therefore, the charge density $\rho_j(\mathbf{r}) = |\psi_j(\mathbf{r})|^2$ of each molecular orbital j transforms according to A_g, so that a transition between two orbitals, e.g., HOMO and LUMO, does not destroy the rectangular symmetry of the total charge density $n(\mathbf{r}) = \Sigma_j n_j \rho_j(\mathbf{r})$; only the occupation numbers n_j are changed. Also subtraction or addition of an electron does not lower the overall symmetry of the charge density of the molecule. Nevertheless, the detailed geometry of the molecule depends on the occupation numbers $\{n_j\}$, and for any fixed set of occupation numbers, the molecule will relax to a different configuration corresponding to the minimum of the total energy.

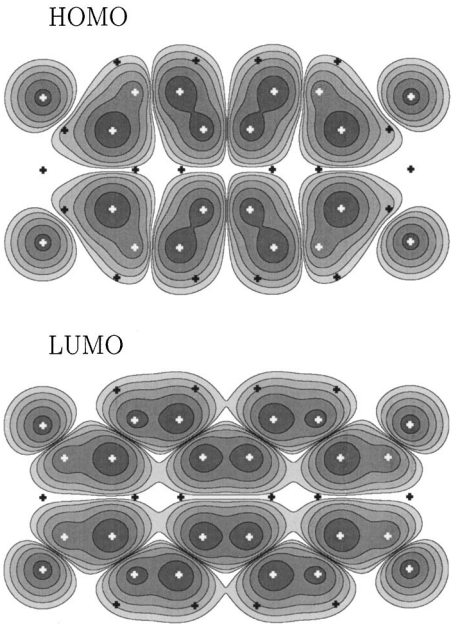

FIG. 1. Geometry of PTCDA in its electronic ground state, and charge density contours of the $A_u(xyz)$ HOMO (upper) and $B_{1g}(yz)$ LUMO (lower), at a distance of one Bohr radius above or below the plane of the molecule. The atomic positions are indicated with crosses, with the three on the lhs and rhs oxygen, and the four upper and four lower hydrogen, surrounding the central carbon network. As both HOMO and LUMO are π orbitals composed of atomic $2p_z$ wave functions, the hydrogen atoms do not contribute. The highest electronic charge density occuring is $|\rho_{max}| = 10^{-1.5} e/a_B^3$, and the charge contours are shown for $|\rho| = 10^{-2.0}$ to $10^{-5.5} e/a_B^3$ in equidistant logarithmic steps. Between consecutive lobes, both the HOMO and the LUMO wave functions change sign.

In order to investigate the geometric changes of a molecule M due to the optical excitation, we calculate the geometries for the ground state $|M\rangle$ and the excited state $|M^*\rangle$ of PTCDA, where an electron has been transferred from the HOMO to the LUMO. As the charge-transfer exciton is discussed in the literature as consisting of a negatively charged central $PTCDA^-$ molecule and a positive charge delocalized over the neighboring molecules in a Wannier-like wave function,[4,24] we investigate also the negatively charged $|M^-\rangle$, where an electron has been added to the LUMO. For these three cases, i.e., neutral PTCDA in its electronic ground and excited state and the molecular anion, the geometry is relaxed in a conjugate gradient scheme based on the DFTB approach, with fixed occupation numbers of the molecular orbitals. The ground-state geometry is shown in Fig.

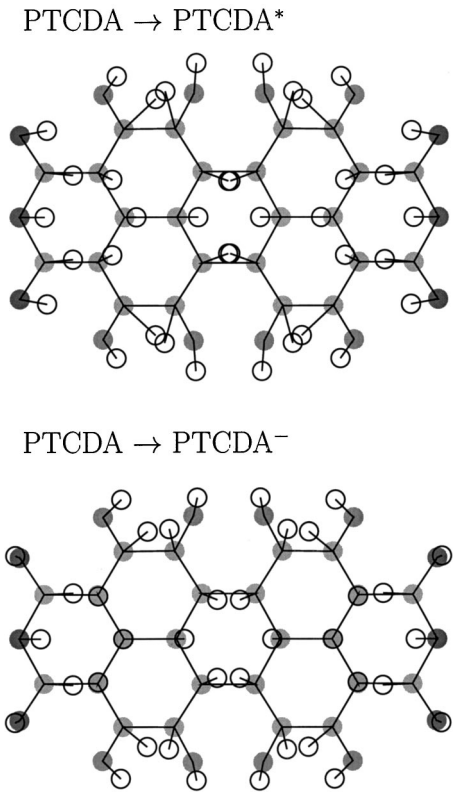

FIG. 2. Deformation patterns of PTCDA* (upper) and $PTCDA^-$ (lower) as compared with the geometry of the molecule in the electronic ground state. Full gray circles correspond to the ground-state geometry, and open circles to the geometry of the deformed PTCDA. In order to make the geometry changes more evident, the deformations have been enlarged by a factor of 40.

1, together with charge-density contours of the $A_u(xyz)$-symmetric HOMO and the $B_{1g}(yz)$-symmetric LUMO, both composed of π-conjugated p_z orbitals. Each orbital can lower its energy by increasing its bonding character between atoms where the wave function has no node, and by decreasing the antibonding character between atoms where a node occurs. This can be achieved by shortening the interatomic distance where the orbital is bonding, and by increasing the interatomic distance where the electronic wave function has an antibonding node. In the electronic ground state, the resulting equilibrium bond lengths have to optimize these electronic requirements for all occupied orbitals together with the short-range repulsive part E_{rep} of the total energy.

When an electron is excited from the HOMO to the LUMO, the electronic requirements on the interatomic distances are changed: The energetically highest occupied electronic LUMO state has now different node planes and bonding regions; see Fig. 1. Therefore, bonds will become shorter where an antibonding node of the HOMO has disappeared, while bonds will become longer where the HOMO had bonding character. With respect to the node planes of the LUMO, the corresponding bonds become longer, and in bonding regions of the LUMO the interatomic distances become shorter. The resulting deformation of the excited $|M^*\rangle$ molecule is shown in Fig. 2, and for each interatomic bond, the expected behavior with respect to the nodes of the HOMO and LUMO wave functions is obtained. Contrary to qualitative patterns discussed elsewhere,[25] in general the direction of the deformations does not coincide with a specific bond direction of the corresponding atom, except obviously for atoms on the x axis. Moreover, each hydrogen follows its carbon neighbor with a similar elongation. We have checked that the atomic elongations in the perylene core of PTCDA are quite similar to a HOMO-LUMO excitation of perylene, explaining also similarities in the Raman spectra; see below.

In the anion $|M^-\rangle$, the overall deformation pattern in Fig. 2 is similar to $|M^*\rangle$, while most deformations are smaller by about a factor $1/\sqrt{2}$. These smaller deformations are easily understood from the fact that in $|M^-\rangle$, only the occupation number of a single orbital is changed, while for $|M^*\rangle$, both the occupation numbers of the LUMO and HOMO are modified by ± 1. However, there are further significant differences in the deformation patterns, e.g., for the C=O double bonds of the carboxylic groups, where both HOMO and LUMO possess a wave function node, so that removing an electron from the HOMO and adding it to the LUMO does not have a significant effect for this interatomic distance in $|M^*\rangle$. For $|M^-\rangle$, on the contrary, the additional electron in the LUMO with its node along these C=O bonds increases the interatomic distance between oxygen and carbon.

Vibrational modes of lower symmetry, e.g., $B_{3g}(xy)$, can contribute to the Raman signals if nearly degenerate electronic transitions with different orientations of the transition dipoles are available. As the HOMO-LUMO excitation is energetically well separated from all other transitions, such processes can contribute only in an off-resonant way to the Raman spectra reported below, resulting in very small Raman cross sections.

C. Elongations of A_g breathing modes

The DFTB method was used to obtain the vibrational modes of PTCDA. From the eigenvectors of the vibrational modes and the deformation patterns in Fig. 2, we can extract a projection on the internal vibrations. Due to the symmetry restrictions and resonance conditions discussed above, only A_g vibrational modes are elongated. It is useful to express the elongation Δq_j between the ground- and excited-state potential minima for each mode $\hbar\omega_j$ in terms of a dimensionless constant $\alpha_j = \sqrt{m\omega_j/(2\hbar)}\Delta q_j$, so that the reorganization energy of each mode is defined as $\lambda_j = m\omega_j^2(\Delta q_j)^2/2 = \alpha_j^2\hbar\omega_j$. The resulting values for λ_j and α_j^2 are given in Table I. For PTCDA*, the reorganization energy is dominated by the C−H stretching modes around 1300 cm^{-1} and the C−C stretching modes close to 1600 cm^{-1}, whereas in terms of normalized reorganization energies α_j^2, also the lowest A_g mode contributes significantly. Comparing $PTCDA^-$ with PTCDA*, the most important change concerns the elongation of the carboxylic stretching mode above 1700 cm^{-1}, directly related to the length change of the corresponding bond in Fig. 2, while most other reorganziation energies are lower by a factor of about 1/2.

In the adiabatic approximation, the electronic ground- and excited-state wave functions can be expressed as products of an electronic and nuclear part. Assuming a single vibronic coordinate for simplicity, and neglecting any dependence of the electronic transition dipole moment on the nucelar position, the vibronic part of the total wave function contributes

TABLE I. A_g breathing modes of PTCDA in the electronic ground state, as calculated with the density-functional tight-binding method: Energies expressed in terms of wave numbers (first column), contribution to the sum of squared displacements of C, H, and O atoms (second to fourth columns), and reorganization energies λ_j and dimensionless elongations α_j^2 due to the optical HOMO-LUMO transition PTCDA→PTCDA* (fifth and sixth column), and due to an additional negative charge PTCDA →PTCDA$^-$ (last two columns).

				PTCDA*		PTCDA$^-$	
$\hbar\omega_j$ (cm^{-1})	$(\delta r_C)^2$ (%)	$(\delta r_H)^2$ (%)	$(\delta r_O)^2$ (%)	λ_j (cm^{-1})	α_j^2 (1)	λ_j (cm^{-1})	α_j^2 1
232	50	7	43	66	0.287	12	0.051
383	22	25	52	3	0.008	32	0.082
474	41	48	11	4	0.008	0	0.000
550	54	33	12	35	0.064	24	0.044
639	45	33	22	34	0.053	3	0.005
728	56	34	11	10	0.013	2	0.002
863	42	56	1	1	0.001	2	0.002
1070	17	80	3	37	0.034	4	0.004
1140	8	91	1	23	0.020	59	0.051
1285	18	81	0	560	0.436	145	0.113
1304	30	69	1	251	0.192	169	0.130
1347	14	86	0	274	0.204	207	0.153
1393	27	73	0	35	0.025	6	0.004
1527	83	16	1	23	0.015	8	0.005
1616	36	64	0	226	0.140	62	0.039
1623	53	46	0	179	0.110	205	0.126
1723	70	2	28	2	0.001	148	0.086
3173	1	99	0	0	0.000	0	0.000
3190	1	99	0	0	0.000	0	0.000

only a Franck-Condon overlap factor. Restricting the discussion to the lowest vibronic level $|0_g\rangle$ of the electronic ground state as the initial state, the probability to excite a transition to the excited-state vibronic level $|n_e\rangle$ with an electric field $\mathbf{E}$ at energy E_L is given by Fermi's golden rule:

$$P(|0_g\rangle\rightarrow|n_e\rangle)=\frac{2\pi}{\hbar}|\mathbf{E}\cdot\boldsymbol{\mu}|^2|\langle 0_g|n_e\rangle|^2 \times\delta(E_L+E_{\mathrm{HOMO}}-E_{\mathrm{LUMO}}-n_e\hbar\omega), \tag{2}$$

where $\boldsymbol{\mu}$ is the electronic transition dipole. It is easily shown that he Franck-Condon factor can be expressed by a Poisson distribution with argument α^2:

$$|\langle 0_g|n_e\rangle|^2=\frac{\alpha^{2n}}{n!}e^{-\alpha^2}. \tag{3}$$

These transition probabilities for a single vibrational mode have to be generalized to the case of the 19 A_g breathing modes elongated due to the HOMO-LUMO excitation of PTCDA.

The Stokes-Raman cross section for each mode $\hbar\omega_j$ measured with an exciting laser energy of E_L can be expressed as[26,27]

$$\sigma_R(\omega_j)\propto\alpha_j^2[1+\langle n(\hbar\omega_j)\rangle] \times|A_0(E_L)-A_0(E_L-\hbar\omega_j)|^2, \tag{4}$$

where $\langle n(\hbar\omega_j)\rangle$ is the thermal occupation of the mode, α_j^2 its normalized reorganization energy, and $A_0(E)$ the Kramers-Kronig transform of the optical absorption spectrum. As usual for the interpretation of resonant Raman spectra, we use only the leading term of the Taylor expansion:

$$\sigma_R(\omega_j)\propto\alpha_j^2[1+\langle n(\hbar\omega_j)\rangle](\hbar\omega_j)^2. \tag{5}$$

Equation (5) will be used in Sec. IV for the interpretation of the measured Raman spectra, and a multi-mode generalization of Eq. (3) including inhomogeneous broadening for the analysis of the optical absorption of dissolved PTCDA in Sec. V.

III. EXPERIMENT

A. Sample preparation

The PTCDA films used in the present study were deposited with organic molecular beam deposition under ultrahigh vacuum conditions at room temperature, using mica (0001) and hydrogen-passivated Si(111) as substrates. A growth rate of about two monolayers per minute was determined by a quartz crystal balance. On the mica substrates, a film thickness of about 20 nm was grown, whereas more than 100 nm PTCDA films were deposited on the passivated silicon substrate. Details of the deposition technique have been described elsewhere.[28–30]

B. Raman scattering geometry

Raman spectra were recorded at room temperature (RT) using a triple monochromator Raman system (Dilor XY) equipped with a charge-coupled device (CCD) camera for multichannel detection that was optically aligned with an ultrahigh vacuum chamber (base pressure $<10^{-10}$ mbar) in which the sample growth was performed.[31] The 2.54 eV (488.0 nm) emission line of an Ar^+ ion laser and the 2.34 eV (530.8 nm) emission line of a Kr^+ ion laser were used for excitation. The monochromator slits were set to a resolution of 1.6 and 1.8 cm^{-1}, respectively. Data were recorded with a data sampling interval of 0.4 cm^{-1} and a Gaussian smoothing with a full width at half maximum (FWHM) of two sampling intervals was applied to the data, resulting in a resolution of 1.8 cm^{-1} and 2.0 cm^{-1}, respectively. During growth, the increasing film thickness was recorded with Raman signals resulting from a laser beam ($P=20$ mW) focused to a spot of about 500 μm in diameter on the sample surface, and for this power density, no degradation of the PTCDA film was observed.[30] The Raman spectra reported in the present work were measured after the growth with a micro-Raman setup with $P<1$ mW focused to a spot diameter of 100 μm. All Raman spectra were recorded in a backscattering geometry.

C. Resonance conditions

The regions of largest absorption of PTCDA (2.5–2.6 eV) and of the charge-transfer exciton[4,6,32,33] (around 2.23 eV)

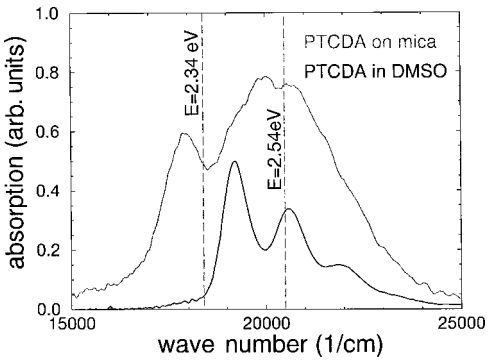

FIG. 3. Optical absorption of PTCDA epitaxial films grown on a mica(0001) substrate (gray) and of PTCDA dissolved in dimethyl sulfoxide (black). The laser lines used for the Raman investigation of PTCDA films grown on H-passivated Si(111) are indicated by broken lines.

were determined for the epitaxial films grown on the transparent mica substrate[9] (see Fig. 3), and the energetic position and shape of the absorption features agree well with literature results.[4,32–34]

In order to take advantage of the signal enhancement in the region of largest absorption in the resonant Raman scattering experiments, the 2.54 eV laser line was used. Superimposed on the Raman lines, a large fluorescence background intensity was observed above 2000 cm^{-1}, which was subtracted from the measured data with an exponential fitting function.

The region of the charge-transfer exciton with its strongest absorption at 2.23 eV was investigated with the 2.34 eV laser line, so that both the laser line (slightly above the absorption maximum) and the inelastically scattered Raman signal (slightly below) are resonantly enhanced. Even though the exponential fluorescence background was stronger than that for the 2.54 eV laser line, the Raman signals could clearly be resolved.

D. Fitting of experimental data

The Raman spectra recorded at $E_L = 2.54$ eV and at $E_L = 2.34$ eV are shown in Fig. 4 and the fingerprint region in Fig. 5. With a nonlinear least-square minimization procedure, a superposition of Lorentzians was fitted to the data; see Tables II to V. Raman peaks with FWHM below about 20 cm^{-1} are interpreted as single-mode spectra, while the larger peaks are two-mode spectra, additionally broadened by the phonon dispersion of the PTCDA film. Where possible, their positions were fixed to sums of single-mode wave numbers. Peaks with large width for at least one laser frequency are interpreted as two-mode structures. The dominating feature at about 520 cm^{-1} corresponds to the optical phonon of the silicon substrate and is reported together with the two-mode peaks.

From Tables II to V and Figs. 4 and 5 it becomes obvious that the main deviations between the Raman signals measured at the two laser energies concern the broad background features, not the sharp single-mode cross sections. This independence of laser energy is in keeping with earlier Raman investigations for films with different morphology on a variety of substrates, and the dominating structures in our Raman spectra occur close to reported positions.[34,35]

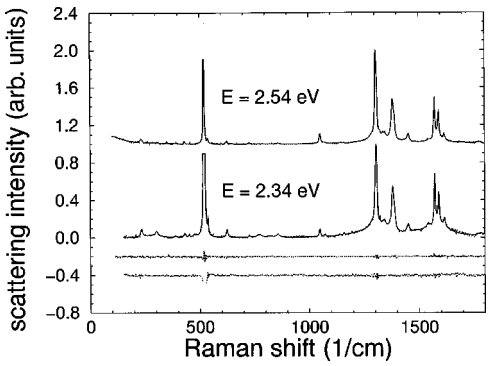

FIG. 4. Resonant Stokes Raman spectra of PTCDA thin films on H-passivated Si(111) substrate (dots), measured with the 2.54 eV ($\lambda = 488.0$ nm, shifted by $+1$ for clarity) and 2.34 eV ($\lambda = 530.8$ nm) laser lines, and superimposed fitting functions based on Lorentzians (solid). The exponential fluorescence background at high energies is subtracted in both cases. The lower curves (dots) are the residuals of the Lorentzian fits, shifted by -0.2 (2.54 eV) and -0.4 (2.34 eV).

IV. COMPARISON OF MEASURED SPECTRA AND THEORY

A. Mode assignment

Successive modes with small energy differences are interpreted as in-phase and out-of-phase superpositions of the same breathing mode patterns on the two PTCDA molecules in the monoclinic unit cell[37] and the lower mode of most pairs has a larger intensity and width. Therefore, their intensities have to be summed up before they can be interpreted with the calculation based on a free PTCDA molecule in Table I; see Table VI.

The small experimental features ($<5\%$ of main peak) between 300 cm^{-1} and 500 cm^{-1} cannot all be assigned to the calculated A_g modes at 383 and 474 cm^{-1}, because the measured data contain several small structures in this region. From polarization-dependent measurements at PTCDA single crystals, the small peaks at 430 cm^{-1} and 451 cm^{-1} are likely to have $B_{3g}(xy)$ symmetry.[36] Compared to the relative cross sections measured at $E_L = 2.54$ eV, they become more pronounced for $E_L = 2.34$ eV. At this lower laser energy, the measured structure at 858 cm^{-1} seems to contain a broader contribution from two-mode scattering (233

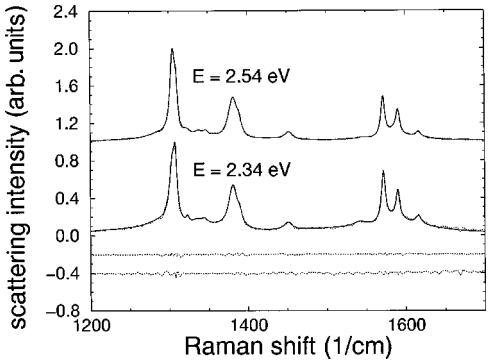

FIG. 5. Detail of resonant Stokes Raman spectra in the fingerprint region, with experimental data (dots), Lorentzian fits (solid), and residuals of the fits (dots).

TABLE II. Narrow features in the Stokes resonant Raman spectra obtained at $E_L = 2.54$ eV. First column: fitted mode energies; second column: Raman cross sections resulting from the fitted Lorentzians, normalized to the sum of the cross sections of the 1304.8 and 1309.1 cm^{-1} modes; third column: FWHM of fitted Lorentzians.

$\hbar\omega_j$ (cm^{-1})	$\sigma_R(\omega_j)$ (1)	FWHM (cm^{-1})
232.2±0.4	0.048±0.008	10.1±1.3
349.5±0.7	0.008±0.013	3.6±3.5
388.8±2.8	0.013±0.010	20.1±8.1
429.5±0.4	0.013±0.005	4.2±1.1
536.8±0.3	0.025±0.005	5.3±0.9
623.8±0.5	0.027±0.006	7.2±1.2
726.7±0.7	0.009±0.005	4.8±1.8
857.5±1.5	0.011±0.006	9.5±4.2
1050.3±0.1	0.101±0.003	8.2±0.2
1069.9±0.7	0.024±0.004	17.7±2.3
1145.7±0.7	0.012±0.003	11.1±2.3
1158.5±0.6	0.004±0.002	4.5±1.7
1304.8±0.1	0.811±0.014	7.6±0.1
1309.1±0.1	0.189±0.012	4.5±0.3
1323.2±0.2	0.086±0.008	11.2±0.8
1337.4±0.3	0.112±0.012	13.0±1.2
1346.6±0.2	0.060±0.009	8.1±1.0
1356.4±0.5	0.039±0.007	14.1±2.0
1381.3±0.1	0.768±0.012	14.1±0.2
1389.1±0.2	0.081±0.010	6.0±0.7
1416.7±1.3	0.020±0.007	13.2±3.6
1432.7±0.2	0.036±0.008	16.0±2.0
1452.1±0.2	0.142±0.010	13.1±0.9
1544.9±0.7	0.022±0.006	13.9±2.9
1571.6±0.1	0.313±0.004	6.0±0.1
1590.4±0.1	0.159±0.008	5.6±0.3
1616.2±0.2	0.030±0.005	5.4±0.8
1773.7±0.7	0.057±0.005	26.0±1.9

TABLE III. As in Table II, but for the broad features in the Stokes resonant Raman spectra obtained at $E_L = 2.54$ eV. Sum frequencies and broadenings kept fixed during the numerical fitting procedure are reported without error margins. The last line corresponds to the silicon optical phonon.

$\hbar\omega_j$ (cm^{-1})	$\sigma_R(\omega_j)$ (1)	FWHM (cm^{-1})
99.6±7.5	1.259±0.119	123.9±7.3
293.6±3.9	0.059±0.020	52.4±15.1
1247	0.225±0.010	96.0±3.5
1286	0.268±0.011	37.5±1.2
1476	0.033±0.001	40
1538	0.168±0.009	80
1586.1±.5	0.226±0.021	20.0±1.2
1615	0.189±0.019	37.6±2.6
1685	0.101±0.006	80
519.4±.1	0.733±0.004	4.0±0.1

TABLE IV. As in Table II, but for the resonant Raman spectra obtained at a laser energy of 2.34 eV, normalized to the sum of the cross sections of the 1304.0 and 1307.8 cm^{-1} modes.

$\hbar\omega_j$ (cm^{-1})	$\sigma_R(\omega_j)$ (1)	FWHM (cm^{-1})
233.2±0.2	0.091±0.006	9.6±0.6
389.6±0.9	0.013±0.005	8.7±2.7
431.0±0.4	0.048±0.006	10.8±1.1
450.8±0.4	0.012±0.004	4.2±1.0
475.9±0.7	0.049±0.008	16.7±2.2
537.3±0.3	0.066±0.014	4.2±0.7
624.6±0.2	0.088±0.004	9.0±0.4
726.7±0.3	0.016±0.003	5.3±0.9
857.5±0.5	0.063±0.007	17.7±1.5
1048.9±0.2	0.062±0.005	6.6±0.4
1072.6±0.5	0.016±0.004	5.7±1.2
1139.3±0.7	0.009±0.004	5.3±1.9
1158.4±0.4	0.013±0.004	4.4±1.1
1304.0±0.3	0.733±0.051	9.8±0.2
1307.8±0.1	0.267±0.035	4.6±0.5
1323.1±0.2	0.046±0.008	5.3±0.8
1334.7±1.2	0.131±0.046	15.3±3.7
1344.7±0.4	0.107±0.016	12.1±1.3
1381.0±0.1	0.760±0.018	13.7±0.3
1389.6±0.2	0.070±0.009	6.1±0.7
1450.8±0.3	0.121±0.007	12.6±0.6
1542.2±0.6	0.108±0.014	18.3±2.1
1571.9±0.1	0.376±0.010	6.0±0.2
1590.0±0.1	.178±0.011	5.3±0.3
1616.0±0.2	.091±0.011	8.7±0.9
1779.5±1.7	.039±0.012	19.5±4.7

+624) or again a B_{3g} mode, so that the cross section in Table IV can be regarded as an upper limit for the A_g single-mode contribution.

For the small peaks at 1323 and 1356 cm^{-1}, no assignment to one of the calculated A_g Raman modes is possible

TABLE V. As in Table III, but for the resonant Raman spectra obtained at a laser energy of 2.34 eV, normalized as the entries of Table IV.

$\hbar\omega_j$ (cm^{-1})	$\sigma_R(\omega_j)$ (1)	FWHM (cm^{-1})
520.0±0.0	2.758±0.013	3.8±0.0
279.2±3.1	0.317±0.026	105.3±6.4
301.5±0.4	0.072±0.009	13.4±1.4
771	0.095±0.007	25.4±1.6
822.8±1.2	0.043±0.008	24.9±4.1
1247	0.925±0.031	158.1±4.6
1286	0.412±0.019	43.3±1.6
1359.3±1.5	0.099±0.033	23.6±7.2
1539	1.829±0.142	220.0±16.1
1586.5±1.0	0.360±0.052	31.4±4.0
1615	0.399±0.075	79.1±12.6
1840	0.415±0.085	44.1±9.0
520.0±0.1	2.758±0.013	3.8±0.1

TABLE VI. Comparison of measured and calculated Raman cross sections, normalized to the largest cross section for the 1305 cm^{-1} mode. First two columns: Raman modes and normalized cross sections measured at $E_L = 2.54$ eV. For the modes near 1054, 1150, 1305, and 1340 cm^{-1}, the positions given are weighted averages over mode pairs in Tables II and IV, the cross sections the corresponding sums. Column 3 and 4: same for $E_L = 2.34$ eV. Column 5: calculated A_g frequencies. Columns 6 and 7: Raman cross sections calculated according to Eq. (5) for PTCDA* (column 6) and negative charging of $PTCDA^-$ (column 7). The average absolute deviation of the calculated mode frequencies is 18 cm^{-1} (rms deviation 24 cm^{-1}).

$\hbar\omega_j$ (cm^{-1})	$\sigma_R(\omega_j)$ (1)	$\hbar\omega_j$ (cm^{-1})	$\sigma_R(\omega_j)$ (1)	$\hbar\omega_j$ (cm^{-1})	$\sigma_R(\omega_j)$ (1)	$\sigma_R(\omega_j)$ (1)
$E_L = 2.54$ eV		$E_L = 2.34$ eV		Calc.	PTCDA*	$PTCDA^-$
232.2±0.4	0.048±0.008	233.2±0.2	0.091±0.006	232	0.032	0.006
388.8±2.8	0.013±0.010	389.6±0.9	0.013±0.005	383	0.002	0.020
429.5±0.4	0.013±0.005	431.0±0.4	0.048±0.006	B_{3g}[36]		
		450.8±0.4	0.012±0.004	B_{3g}[36]		
		475.9±0.7	0.049±0.008	474	0.003	0.000
536.8±0.3	0.025±0.005	537.3±0.3	0.066±0.014	550	0.029	0.020
623.8±0.5	0.027±0.006	624.6±0.2	0.088±0.004	639	0.032	0.003
726.7±0.7	0.009±0.005	726.7±0.3	0.016±0.003	728	0.010	0.002
857.5±1.5	0.011±0.006	857.5±0.5	0.063±0.007	863	0.001	0.003
1054.1±0.2	0.125±0.004	1053.6±0.2	0.078±0.006	1070	0.055	0.006
1149.1±0.7	0.016±0.004	1150.5±0.5	0.022±0.006	1140	0.036	0.093
1305.6±0.1	1.000±0.019	1305.0±0.2	1.000±0.072	1285	1.000	0.259
1340.6±0.2	0.171±0.017	1339.2±0.7	0.238±0.065	1304	0.454	0.306
1381.3±0.1	0.768±0.012	1381.0±0.1	0.760±0.018	1347	0.513	0.386
1389.1±0.2	0.081±0.010	1389.6±0.2	0.070±0.009	1393	0.067	0.011
1416.7±1.3	0.020±0.007					
1432.7±0.2	0.036±0.008					
1452.1±0.2	0.142±0.010	1450.8±0.3	0.121±0.007			
1544.9±0.7	0.022±0.006	1542.2±0.6	0.108±0.014	1527	0.048	0.017
1571.6±0.1	0.313±0.004	1571.9±0.1	0.376±0.010	1616	0.506	0.140
1590.4±0.1	0.159±0.008	1590.0±0.1	0.178±0.011	1623	0.402	0.461
1616.2±0.2	0.030±0.005	1616.0±0.2	0.091±0.011			
1773.7±0.7	0.057±0.005	1779.5±1.7	0.039±0.012	1723	0.004	0.353

because they are already needed for the interpretation of larger experimental features. However, as they are close to the average wave number of the larger Raman peaks around them, they could result from a superposition of these nondegenerate modes on the two molecules of the monoclinic unit cell. These modes are skipped in the comparison between experiment and theory in Table VI.

The modes at 1433, 1451, and 1616 cm^{-1} cannot be assigned to A_g breathing modes. Tentatively, we interpret them as second-order scattering processes of lower modes, i.e., the second harmonic of the two most pronounced out-of-plane dipole active modes at 734 and 809 cm^{-1}.[9,34] A further possibility is that the observed 1616 cm^{-1} Raman mode corresponds to one of the strongest B_{3g}-symmetric modes of perylene observed at 1622 cm^{-1}.[38] The relative cross sections at the two different laser energies support this argument; see the discussion of the B_{3g} features at 430 and 451 cm^{-1} above.

B. Deformation patterns of selected modes

From the calculation of the vibrational eigenvectors, we can assign each of the dominating Raman modes to different parts of the deformation pattern for optical excitation HOMO → LUMO; see Figs. 6 and 7. The elongation of the lowest-frequency mode corresponds to the in-phase shortening of the molecule, which is due to the vanishing of the node lines of the HOMO along the *y* axis, as can be seen by comparing Figs. 1 and 2. The new node lines of the LUMO are responsible for the increased width of the excited molecule, resulting in the elongations of the 537 cm^{-1} and 624 cm^{-1} modes. The frequency difference between these two is easily understood from their elongation patterns, shown in Fig. 6: The lower-mode energy corresponds to an in-phase expansion that is close to radial, while the higher mode has already some out-of-phase tangential character, resulting in an increased frequency.

Figure 7 shows the three high-frequency vibrations dominating the Raman spectrum. For these modes, the elongations along most C−C bonds correspond to the increase and decrease of the interatomic distances of PTCDA* in Fig. 2. While the modes at 1305 cm^{-1} and 1382 cm^{-1} contain large contributions of C−H in-plane bending elongations, the elongation pattern of the 1572 cm^{-1} mode is dominated by C−C stretching and corresponds to the optical phonon of graphite at the Γ point of the Brillouin zone, explaining the similarity in frequency. For the 1590 cm^{-1} mode (not shown), the pattern is again dominated by C−C stretching,

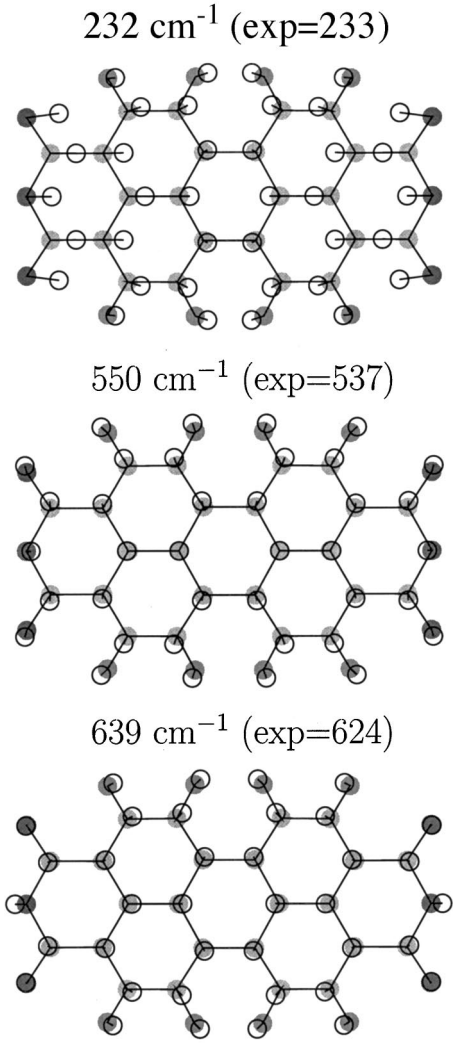

FIG. 6. Calculated elongation patterns of the three dominating low-frequency Raman modes. From top to bottom: 232 (exp, 233), 550 (exp, 537), 639 (exp, 624) cm^{-1}. The contribution of each mode to the total deformation of PTCDA* is enlarged by a factor of 40.

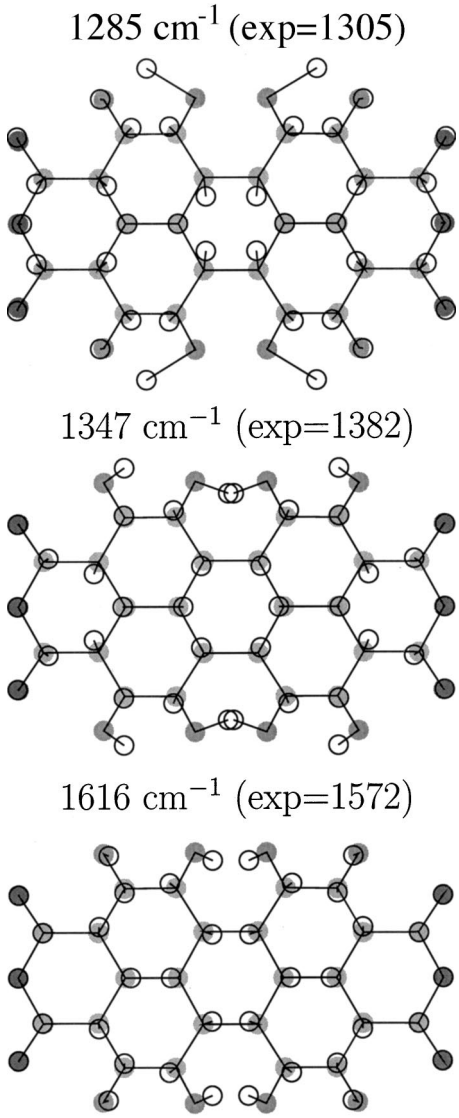

FIG. 7. As Fig. 6, but for the three dominating high-frequency Raman modes. From top to bottom: 1285 (exp, 1305), 1347 (exp, 1382), 1616 (exp, 1572) cm^{-1}.

but no simple correspondence with the graphite unit cell is found. As the total deformation pattern of PTCDA* in Fig. 2 does not contain any pronounced C−H bending, the corresponding parts summed over the vibrational eigenmodes in Fig. 7 cancel approximately.

Depending on the substrate, a pronounced splitting of the C=O breathing mode around 1774 cm^{-1} of about 15 wavenumbers can be observed, interpreted again as a splitting due to the two molecules in the crystal unit cell. This splitting is also observed for the C=O features dominating the infrared spectra.[9] With the signal-to-noise ratio of the resonant Raman scattering data reported here, this splitting could not be confirmed, but it is likely to be the reason for the relatively large full width at half maximum (FWHM) of the C=O mode reported in Tables II and IV.

C. Comparison of measured and calculated scattering cross sections

The experimental and calculated cross sections are reported in Table VI, and for all the 17 A_g Raman modes below 2000 cm^{-1}, we achieve a one-to-one correspondence with measured features. Surprisingly, we find a striking agreement of the measured A_g Raman intensities in the fingerprint region (1250–1650 cm^{-1}) for the two laser energies $E_L = 2.34$ eV and 2.54 eV, and the systematic deviation for the low-frequency modes is interpreted in terms of changes of the polarizabilities A_0 in Eq. (4), so that we do not believe that the elongations α^2 of the Raman modes differ by this factor of about 2. Referring to the intensities calculated for the excitation of a neutral PTCDA molecule, PTCDA→PTCDA*, we find generally a good agreement within reasonable error margins, especially with the cross sections resulting at the larger laser energy of 2.54 eV. In this broad and structureless absorption band, the polarizability A_0 is smoother than close to the sharp absorption peak at lower energy, so that the approximations involved in Eq. (5) used for the calculated intensities are better satisfied. However, the systematic increase of the scattering cross sections for the low-frequency modes measured at $E_L = 2.34$ eV indicates that a more precise inclusion of the energy dependence

of the polarizability would be desirable. While the relative cross sections of the C−H bending modes in the region 1300–1400 cm^{-1} are in reasonable agreement with the measured data, the cross sections of the C-C stretching modes near 1600 cm^{-1} are overestimated by a factor of about 2 compared to the C−H bending modes. In both regions, we observe a small redistribution between cross sections of consecutive modes: The mode at 1304 (experimental 1340) cm^{-1} and the mode at 1623 (experimental 1590) gain intensity with respect to their neighbors. The intensity of the carboxylic bond at 1723 (experimental about 1775) cm^{-1} remains quite small both in the experiment and in the calculation.

While systematic deficiencies of the DFTB calculation are difficult to estimate, there could also be some deviations related to the difference between an isolated molecule and the monoclinic epitaxial films, as is also obvious from the symmetry lowering of the molecular geometry.[21,22] Details of geometrical changes could have some influence on the vibrational frequencies and eigenvectors, and the distribution of the HOMO and LUMO over the molecule could be affected, resulting in minor changes of the projections of the deformation on the vibronic eigenstates. Even though the scatter of our calculated mode frequencies is larger than in recent B3LYP DFT calculations for polycyclic aromatic hydrocarbons,[38,40] they are slightly more precise than those in previous calculations for PTCDA,[39] and the reliability of our calculated Raman cross sections is similar.

D. Absence of net charge transfer

The Raman cross sections resulting from the deformation of a molecule with an additional negative charge is in poor agreement with the measured data at both laser energies; see Table VI. Even though the contribution from the surrounding molecules with the corresponding positive charge is not included in this calculation, some Raman modes would give already a much larger cross section for the deformation PTCDA→$PTCDA^-$ of the negatively charged molecule alone, especially the 1150 cm^{-1} (calculated 1140) mode and the C=O modes around 1770 cm^{-1} (calculated 1723): The C=O mode would become a dominating feature due to the bond stretching corresponding to the repulsive node of the LUMO; see Figs. 1 and 2. This intensity would even increase when the deformation of the surrounding positively charged molecules would be included because the subtraction of a HOMO electron would remove a repulsive node, resulting in a significant compression of the C=O bond for $PTCDA^+$ and a corresponding Raman contribution. From the very weak measured Raman cross section of this mode, we conclude that no significant net charge transfer occurs in the region of the charge-transfer exciton. However, as the most general excited state of two PTCDA molecules is of the type $a|M^*M\rangle + b|MM^*\rangle + c|M^+M^-\rangle + d|M^-M^+\rangle$, this does only require $|c|^2 \approx |d|^2$, not $|c|^2 + |d|^2 \ll |a|^2 + |b|^2$. Therefore, the absence of net charge transfer indicated by our Raman spectra is not in contradiction with the applicability of charge-transfer models both to optical absorption[25] and electroabsorption[7] of PTCDA.

E. Comparison with Raman spectra of perylene and poly-peri-naphthalene

As PTCDA and perylene differ only by the end groups of the molecule, many geometrical and dynamic features show strong analogies. We have checked that our calculated total deformation patterns of the excited state of perylene and PTCDA are quite similar. For most of the A_g elongation patterns of PTCDA shown in Figs. 6 and 7, a close resemblance with perylene A_g modes can be found; compare recent corrected B3LYP DFT calculations[38,40,41] and experimental data.[38] The lowest PTCDA A_g mode at 233 (calculated 232) cm^{-1} has a comparable pattern as the lowest perylene mode observed at 357 (Ref. 38) [calculated 352 (Ref. 40)], the frequency change being related to the heavy carbon-oxygen end groups. Concerning the PTCDA mode observed at 537 (549) cm^{-1}, a similar mode pattern occurs in perylene at 549 (547) cm^{-1}. The dominant PTCDA C−H bending mode at 1305 (1285) cm^{-1} corresponds to the 1298 (1299) cm^{-1} mode in perylene, while the three consecutive modes for PTCDA are not directly comparable to perylene, even though the mixed C−H bending and C−C stretching character is similar. The deformation pattern of the PTCDA C−C stretching mode at 1572 (1616) cm^{-1} agrees again nicely with the 1569 (1571) cm^{-1} perylene mode. Concerning the A_g Raman cross sections, perylene is dominated by the modes at 1298, 1374, and 1569 cm^{-1}, with a somewhat larger scattering of the C−C stretching mode at 1569 cm^{-1} mode compared to PTCDA. The scatter of the calculated Raman cross sections for perylene with respect to the oberved ones[38,40] is similar to the results we present for PTCDA.

Poly-peri-naphthalene (PPN) consists of a one-dimensional repetition of naphthalene groups, corresponding to the strongly conjugated building blocks of both perylene and PTCDA. The most important deformations related to the relaxed excited state of PTCDA and perylene occur in the naphthalene blocks; see Fig. 2. Therefore, the Raman spectra of the one-dimensional analogon PPN are dominated by similar features around 1290, 1360, and 1570 cm^{-1},[42] and it was demonstrated that PTCDA deposition at high substrate temperatures[43] or under high laser fluence[44] results in polymerization, so that the resulting Raman spectra are similar to PPN in both cases. Actually, a precursor of the broadened Raman features in the polymer is already visible in the form of additional modes for conjugated molecules containing an increasing number of naphthalene groups; see, e.g., the differences between naphthalene and perylene[38] and between perylene and terrylene.[19] As was discussed recently in some detail, the strong similarities between different polycyclic aromatics based on naphthalene groups and PPN can be understood in terms of the Hückel and Pariser-Parr-Pople models, determining both the electronic states and the qualitative deformation patterns.[45]

V. LINEAR ABSORPTION OF PTCDA IN DIMETHYL SULFOXIDE SOLUTION

In order to investigate the absorption properties of single PTCDA molecules, it is necessary to dissolve them in an adapted solvent. For the case of dimethyl sulfoxide (DMSO), already a solution containing a concentration of about 1 μM

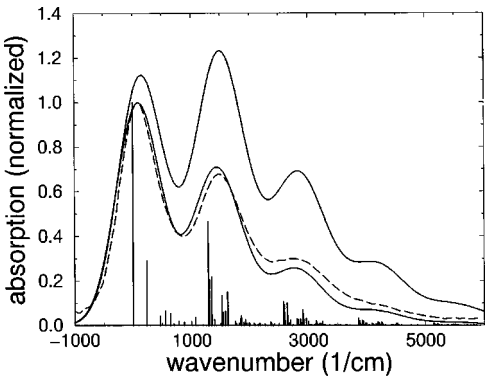

FIG. 8. Optical absorption of PTCDA. Dashed line, experimental absorption signal in $0.2\mu M$ solution of PTCDA in DMSO, shifted down by 2.37 eV. Discrete vertical lines, calculated Poisson distribution over A_g modes and their harmonics, normalized to the intensity of the 0-0 transition. Solid lines, corresponding absorption spectra including a Gaussian broadening of FWHM=850 cm^{-1} according to $\alpha=\omega\epsilon''/nc$, where ω refers to the sum of the vibronic part shown and the electronic gap of 2.37 eV for PTCDA in DMSO. Upper solid line, with α_j^2 as calculated; lower, with all α_j^2 reduced to $0.65\alpha_j^2$. For the prefactor ω in the formula for the absorption, the LDA electronic gap of 1.79 resulting from the DFTB calculation was corrected to the experimental value of 2.37 eV in DMSO.

PTCDA shows some bulk features in the region of the charge-transfer exciton.[6] Therefore, much lower concentrations are needed for any investigation of well-dissolved isolated molecules. The experimental data reported in Fig. 8 were measured at a concentration of 0.2 μM. For the calculated curves in Fig. 8, the well-known gap error of density-functional theory was corrected together with solvent-dependent renormalizations of the electronic gap. Except for a necessary reduction of the calculated elongations, we find good agreement with the observed vibrational structure, so that the separation of the consecutive bands in the vibronic progression can be interpreted as an average of the vibrational frequencies of the most prominent Raman modes. This is in keeping with earlier calculations of the elongations of the A_g modes during optical absorption,[39] so that configuration coordinate diagrams based on a single effective internal mode[6] can be ruled out. We interpret the reduced elongations in the dissolved molecule as an effect of the high dielectric constant of the solvent. Under optical excitation of PTCDA, the change of the electronic charge density leads to a displacement field **D** within the PTCDA molecule. The resulting electric field **E** and the corresponding forces on the atomic cores are reduced due to screening of **D** by the solvent polarization. Even though the dielectric function of DMSO is very high, the reduction of the reorganization energies by a factor of only about 0.65 is probably due to the nonlocal nature of the screening, so that the deformation of the PTCDA molecule is still rather similar to the isolated molecule. Obviously, the same reduction for the elongations of all modes gives only a first estimate, as any screening effect would depend on the position of the atoms involved in each vibrational pattern.

VI. CONCLUSION

Our results for the deformation of an isolated PTCDA molecule from the electronic ground state to the relaxed excited state of neutral PTCDA show good agreement with the experimental Raman spectra obtained on epitaxial films, and the vibrational structure in linear absorption of PTCDA dissolved in DMSO can be interpreted in terms of an average of the most prominent Raman lines elongated due to the HOMO-LUMO excitation. However, we find no correspondence of resonant Raman spectra recorded in the region of the charge-transfer exciton with the calculated deformation of the molecule due to an additional negative charge. Instead, these Raman spectra agree quite well with the data measured at higher laser energy. This leads us to the conclusion that a significant net charge separation during optical excitation in this energy region is highly unlikely.

ACKNOWLEDGMENTS

We would like to thank T. Fritz (Dresden) for the epitaxial PTCDA films on the mica substrate and M. Hoffmann (Dresden) for the absorption measurement of PTCDA dissolved in DMSO. Financial support by the Deutsche Forschungsgemeinschaft is gratefully acknowledged.

[1] C.W. Tang and S.A. van Slyke, Appl. Phys. Lett. **51**, 913 (1987).
[2] P.E. Burrows and S.R. Forrest, Appl. Phys. Lett. **62**, 3102 (1993).
[3] R.T. Tayler, P.E. Burrows, and S.R. Forrest, IEEE Photonics Technol. Lett. **9**, 365 (1997).
[4] S.R. Forrest, Chem. Rev. **97**, 1793 (1997), and references therein.
[5] P. Fenter, P. Eisenberger, P. Burrows, S.R. Forrest, and K.S. Liang, Physica B **221**, 145 (1996).
[6] V. Bulovic, P. Burrows, S.R. Forrest, J.A. Cronin, and M.E. Thompson, Chem. Phys. **210**, 1 (1996).
[7] E. Haskal, Z. Shen, P.E. Burrows, and S.R. Forrest, Phys. Rev. B **51**, 4449 (1995).
[8] U. Gomez, M. Leonhardt, H. Port, and H.C. Wolf, Chem. Phys. Lett. **268**, 1 (1997).
[9] R. Kaiser, M. Friedrich, T. Schmitz-Hübsch, F. Sellam, S. Hohenecker, T.U. Kampen, K. Leo, and D.R.T. Zahn, Fresenius J. Anal. Chem. **363**, 189 (1999).
[10] M. Elstner, D. Porezag, G. Jungnickel, J. Elsner, M. Haugk, Th. Frauenheim, S. Suhai, and G. Seifert, Phys. Rev. B **58**, 7260 (1998).
[11] D. Porezag, Th. Frauenheim, Th. Köhler, G. Seifert, and R. Kaschner, Phys. Rev. B **51**, 12 947 (1995).
[12] J.P. Perdew, K. Burke, and M. Ernzerhof, Phys. Rev. Lett. **77**, 3865 (1996).
[13] J.S. Dewar, E. Zoebisch, E.F. Healy, and J.J. Stewart, J. Am. Chem. Soc. **107**, 3902 (1985).
[14] J.A. Pople, H.B. Schlegel, R. Krishnan, D.J. Defrees, J.S. Binkley, M.S. Frisch, R.A. Whiteside, R.F. Hout, and W.J. Hehre, Int. J. Quantum Chem., Quantum Chem. Symp. **15**, 269 (1981).
[15] M. Jung, U. Baston, G. Schnitzler, M. Kaiser, J. Papst, T. Porwol, H.J. Freund, and E. Umbach, J. Mol. Struct. **293**, 239 (1993).
[16] C. Kendrick, A. Kahn, and S.R. Forrest, Appl. Surf. Sci. **104/105**, 586 (1996).

[17] M.R. Pederson and C.C. Lin, Phys. Rev. B **35**, 2273 (1987).
[18] D.V. Porezag and M.R. Pederson, Phys. Rev. B **54**, 7830 (1996).
[19] M. Rumi, G. Zerbi, and K. Müllen, J. Chem. Phys. **108**, 8662 (1998).
[20] E. Hädicke and F. Graser, Acta Crystallogr., Sect. C: Cryst. Struct. Commun. **42**, 189 (1986); *ibid.*, **42**, 195 (1986).
[21] M.L. Kaplan, C.S. Day, A.J. Lovinger, P.H. Schmidt, and S.R. Forrest (private communication).
[22] Datafile in CSD (Cambridge Structure Database) format written by T. Fritz, based on the data of Ref. 21.
[23] R. Scholz *et al.* (unpublished).
[24] M. Pope and C.E. Swenberg, *Electronic Processes in Organic Crystals* (Clarendon Press, Oxford, 1982).
[25] M.H. Hennessy, Z.G. Soos, R.A. Pascal, and A. Girlando, Chem. Phys. **245**, 199 (1999).
[26] A.B. Myers and R.A. Mathies, in *Biological Applications of Raman Spectroscopy*, edited by T.G. Spiro (Wiley, New York, 1987), Vol. 2, p. 1.
[27] F. Markel, N.S. Ferris, I.R. Gould, and A.B. Myers, J. Am. Chem. Soc. **114**, 6208 (1992).
[28] T. Schmitz-Hübsch, T. Fritz, F. Sellam, R. Staub, and K. Leo, Phys. Rev. B **55**, 7972 (1997).
[29] S. Hohenecker, D. Drews, M. Lübbe, D.R.T. Zahn, and W. Braun, Appl. Surf. Sci. **123/124**, 585 (1998).
[30] T.U. Kampen, D.A. Tenne, S. Park, G. Salvan, R. Scholz, and D.R.T. Zahn, Phys. Status Solidi B **215**, 431 (1999).
[31] V. Wagner, D. Drews, N. Esser, D.R.T. Zahn, and W. Richter, J. Appl. Phys. **75**, 7330 (1994).
[32] S.R. Forrest, M.L. Kaplan, and P.H. Schmidt, J. Appl. Phys. **55**, 1492 (1984).
[33] V. Bulović and S.R. Forrest, Chem. Phys. **210**, 13 (1996).
[34] K. Akers, R. Aroca, A.-M. Hor, and R.O. Loutfy, J. Phys. Chem. **91**, 2954 (1987).
[35] U. Guhathakurta-Gosh and R. Aroca, J. Phys. Chem. **93**, 6125 (1989).
[36] D.A. Tenne, S. Park, T.U. Kampen, A. Das, R. Scholz, and D.R.T. Zahn, Phys. Rev. B (to be published).
[37] A.J. Lovinger, S.R. Forrest, M.L. Kaplan, P.H. Schmidt, and T. Venkatesan, J. Appl. Phys. **55**, 476 (1984).
[38] H. Shinohara, Y. Yamakita, and K. Ohno, J. Mol. Struct. **442**, 221 (1998).
[39] K. Gustav, M. Leonhardt, and H. Port, Monatsh. Chem. **128**, 105 (1997).
[40] K.K. Ong, J.O. Jenssen, and H.F. Hameka, J. Mol. Struct.: THEOCHEM **459**, 131 (1999).
[41] A.D. Becke, Phys. Rev. A **38**, 3098 (1988); C. Lee, W. Yang, and R. G. Parr, *ibid.*, **37**, 785 (1988).
[42] M. Murakami, S. Ijima, and S. Yoshimura, J. Appl. Phys. **60**, 3856 (1986).
[43] H. Kamo, M. Yudasaka, S. Kurita, T. Matsui, R. Kikuchi, Y. Ohki, and S. Yoshimura, Synth. Met. **68**, 61 (1994).
[44] M. Yudasaka, Y. Tasaka, M. Tanaka, H. Kamo, Y. Ohki, S. Osami, and S. Yoshimura, Appl. Phys. Lett. **64**, 3237 (1994).
[45] Z.G. Soos, M.H. Hennessy, and G. Wen, Chem. Phys. Lett. **274**, 189 (1997).